Flux-driven simulations of turbulence collapse

G. Y. Park, S. S. Kim, Hogun Jhang, P. H. Diamond, T. Rhee, and X. Q. Xu

Flux-driven simulations of turbulence collapse

G. Y. Park,[1] S. S. Kim,[1] Hogun Jhang,[1] P. H. Diamond,[1,2] T. Rhee,[1] and X. Q. Xu[3]

[1]*National Fusion Research Institute, Daejeon 305-333, South Korea*
[2]*CASS and Department of Physics, University of California, San Diego, La Jolla, California 92093-0429, USA*
[3]*Lawrence Livermore National Laboratory, Livermore, California 94551, USA*

Using three-dimensional nonlinear simulations of tokamak turbulence, we show that an edge transport barrier (ETB) forms naturally once input power exceeds a threshold value. Profiles, turbulence-driven flows, and neoclassical coefficients are evolved self-consistently. A slow power ramp-up simulation shows that ETB transition is triggered by the turbulence-driven flows via an intermediate phase which involves coherent oscillation of turbulence intensity and $E \times B$ flow shear. A novel observation of the evolution is that the turbulence collapses and the ETB transition begins when $R_T > 1$ at $t = t_R$ (R_T: normalized Reynolds power), while the conventional transition criterion ($\omega_{E \times B} > \gamma_{lin}$ where $\omega_{E \times B}$ denotes mean flow shear) is satisfied only after $t = t_C$ ($> t_R$), when the mean flow shear grows due to positive feedback. © 2015 AIP Publishing LLC. [http://dx.doi.org/10.1063/1.4914841]

I. INTRODUCTION

Turbulence normally degrades the confinement of particles and heat in magnetically confined plasmas, as input power increases. Once the input power exceeds a threshold value, however, plasmas suddenly bifurcate to a high confinement mode (H-mode) by the formation of an edge transport barrier (ETB). Since its discovery in the ASDEX tokamak,[1] the H-mode has been reproduced in many toroidal systems and is important as a baseline operating scenario for ITER. The H-mode is attributed to the suppression of turbulence by $E \times B$ flow shear.[2,3] However, the mechanism of the L → H transition remains an open question. Results from several recent experiments have reinforced the suggestion that turbulence-driven flows trigger the H-mode transition.[4–7] A limit cycle oscillation (LCO) regime is observed before the transition, implying the existence of self-regulating interaction between the turbulence and the flow.[8,9] A quantitative transition criterion has been suggested. The criterion is that the normalized Reynolds power $R_T > 1$. Here, R_T is a ratio of the Reynolds stress mediated transfer of turbulence energy into the flow to the rate of energy input into the turbulence. Identification of the importance of the $R_T > 1$ criterion opens new pathways toward the understanding of empirical power threshold scaling trends. More generally, the type of zonal flow-mediated transport bifurcations discussed here is relevant to all systems where the potential vorticity mixing is an important physical process.[10]

Although many theoretical and simulation works have contributed to the understanding of the L → H transition mechanism,[2,11–17] a successful self-consistent simulation model which can capture the basic physics of the L → H transition has not yet been realized. In this paper, we report on nonlinear three-dimensional fluid simulations which elucidate the dynamics and evolution of ETB formation. Self-consistent flux-driven simulation results are presented which explicitly demonstrate ETB formation when input power is above a threshold power (Sec. III), and thus reproduce recent results of ETB formation[18] on the basis of a similar numerical model. In the present study, special attention is focused on the role of turbulence-driven flows and associated transition criterion $R_T > 1$ for ETB formation and the detailed transition time sequence (Sec. IV). Note that Ref. 18 did not quantitatively address these important elements of the transition physics. Our simulations can help to address and resolve some disagreements between current experiments. In particular, the questions of the temporal sequence and causality lie at the heart of an ongoing controversy in the literature concerning the L → H transition. While some experiments[4,5,7,9] suggest that significant zonal flow growth by Reynolds work precedes, and in fact triggers, the L → H transition, others[19,20] suggest that the mean $E \times B$ flow evolution leads that of the zonal flow.

II. SIMULATION MODEL

As a self-consistent numerical model, we employ electrostatic resistive ballooning turbulence, but the results are generic to all models of turbulence in confined plasmas. The basic equations are the vorticity ($\nabla \cdot \mathbf{J} = 0$, $\mathbf{J}$: the plasma current density) and pressure advection equations.[21] The normalized form of these equations is

$$\frac{\partial U}{\partial t} = -\mathbf{V}_{E \times B} \cdot \nabla U - B^2 \nabla_{||} \frac{J_{||}}{B} + \mathbf{b} \times \kappa \cdot \nabla P + \mu_{\perp} \nabla_{\perp}^2 U$$
$$- \mu_{neo}(U_{0,0} - U_P),$$

$$\frac{\partial P}{\partial t} = -\mathbf{V}_{E \times B} \cdot \nabla P + \chi_{||} \nabla_{||}^2 P + \chi_{\perp} \nabla_{\perp}^2 P + S_0 - S_1 P_{0,0},$$

$$(1)$$

where $U = \nabla_{\perp}^2 \phi$, $\mathbf{V}_{E \times B} = \mathbf{b} \times \nabla \phi$, $J_{||} = S \nabla_{||} \phi$, $\kappa = \mathbf{b} \cdot \nabla \mathbf{b}$ is the magnetic curvature, $U_{0,0}(P_{0,0})$ is the $(m, n) = (0, 0)$ component of $U(P)$, $U_P = -\delta(1 - k_{neo}) \nabla_{\perp}^2 P_{0,0} + \delta \nabla_{\perp} k_{neo} \cdot \nabla_{\perp} P_{0,0}$ (k_{neo} is the neoclassical flow coefficient). $S = \mu_0 R_0 V_A / \eta$ (V_A: Alfven velocity, η: resistivity, R_0: major radius) and $\delta = V_A / 2 \omega_{ci} R_0$ are the Lundquist number and

diamagnetic factor, respectively. Potential ϕ, pressure P, length, and time are normalized to $V_A R_0 B$, $B_0^2/2\mu_0$, R_0, and $\tau_A = R_0/V_A$, respectively. In our model, density is set to be constant ($=10^{19} \text{m}^{-3}$) and a fixed ratio between electron and ion temperatures is assumed and taken to be one. The last term on the right-hand side of Eq. (1) (μ_{neo}: neoclassical friction coefficient) is obtained from the radial force balance equation linking the radial electric field, pressure gradient, and poloidal velocity (detailed derivation can be found, for example, in Ref. 22). This term gives rise to mean $\boldsymbol{E} \times \boldsymbol{B}$ flow generation due to pressure curvature. This formulation is based on an *ad-hoc* closure (or a heuristic closure as in Ref. 23) for the neoclassical parallel viscosity which is strictly valid for time scale larger than an ion collisional time.[24] For simplicity, we neglect here the contribution from the radial derivative of toroidal rotation. Thus, all aspects of toroidal rotation and parallel flow are neglected. We understand that this additional contribution to mean $\boldsymbol{E} \times \boldsymbol{B}$ flow generation could be important in some cases (i.e., when there is strong toroidal rotation shear), and thus additional efforts to understand these effects are worth pursuing in the future. S_0 and $S_1 P_{0,0}$ represent pressure source and sink terms, respectively. Perpendicular and parallel diffusivities ($\chi_\perp, \chi_\parallel, \mu_\perp$) are also included. In the simulations, we use $S = 10^5$, $\chi_\parallel = 0.1$, $\chi_\perp = \mu_\perp = 3.0 \times 10^{-6}$. For these values, the resulting turbulent transport coefficient $\chi_{turb} \simeq 10\chi_\perp$ before transition. Here, $\chi_{turb} = -1.5\langle \tilde{v}_r \tilde{p} \rangle / \nabla p$, where the tildes indicate fluctuating quantities (in time and space), and the brackets stand for an average in the poloidal and toroidal directions. A shifted circle cross-section equilibrium is used in the simulations with the following parameters: minor radius is $1.2\,\text{m}$, $R_0 = 3.4\,\text{m}$, and $B_0 = 2\,\text{T}$. Our simulation covers a radial extent between $x = 0.4$ and 1.2, where x is the normalized poloidal flux ($x = 0$ and 1 correspond to the magnetic axis and plasma boundary, respectively). For radial boundary conditions, the Dirichlet condition is employed except that the Neumann boundary condition is used for $P_{0,0}$ on the inner radial boundary ($\partial P_{0,0}/\partial x = 0$ on $x = 0.4$). The definition of the plasma boundary ($x = 1$) is somewhat arbitrary here since there is no true scrape-off layer (SOL) in our simulations, and so $x = 1$ is defined as the point beyond which pressure sink (S_1) is increased abruptly (see Fig. 1(b)). The simulations are carried out using the BOUT++ (Ref. 25) framework. We note here that a previous simulation study using BOUT has implemented more sophisticated SOL model[26] and recovered aspects of ETB formation though a detailed physics analysis of transport bifurcation was not performed.[27] To do this, a simpler model, but one containing necessary physics ingredients, is more useful.

Figure 1(a) shows the radial profiles of k_{neo} and μ_{neo} obtained at one particular time from the present simulation. In the simulation, k_{neo} and μ_{neo} are determined self-consistently using the pressure profile dependence of the collisionality parameter $\nu_{i,*}$ (since $\nu_{i,*} \sim nT_i^{-2} \sim p^{-2}$ with constant density in our model) as pressure profiles evolve in time. To evaluate k_{neo} and μ_{neo} as a function of $\nu_{i,*}$, the Hinton and Hazeltine formula is used for $k_{neo}(\nu_{i,*})$[28] and an approximate fitting formula for $\mu_{neo}(\nu_{i,*})$ is taken from
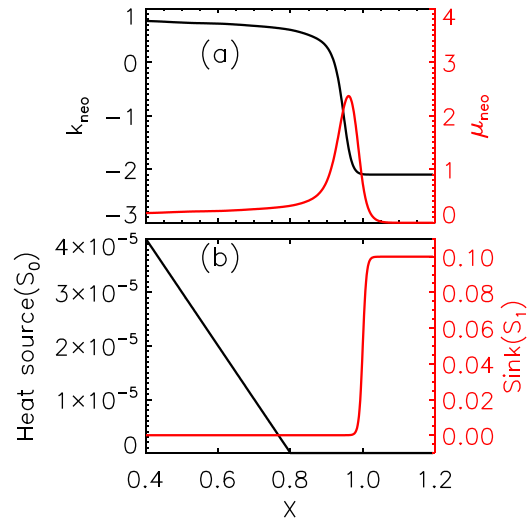

FIG. 1. Profiles of k_{neo} and μ_{neo} (a), and S_0 and S_1 (b).

Ref. 29. The values of $\nu_{i,*}$ and μ_{neo} at $x = 0.4$ are set to 0.2. Notice that collisionality in our simulation satisfies $0.1 < \nu_{i,*} < 100$ (banana to collisional regime) along the radial direction with this setting of $\nu_{i,*}$ at $x = 0.4$, which represents a typical value of L-mode at the tokamak edge. As can be seen from Figure 1(a), k_{neo} (μ_{neo}) rapidly decreases (increases) toward plasma boundary ($x = 1$). Figure 1(b) shows the radial profiles of heat source (S_0) and sink (S_1) profiles used in the present simulation.[30]

III. ETB FORMATION PHENOMENOLOGY

For the ETB formation study, we initialize the plasma profile with a mild slope, and then evolve the system at a constant power until after it reaches a steady state profile. The time required to reach the steady state is about $2000\tau_A$ and is typically much larger than the turbulence correlation time, whose value is about $150\tau_A$. In steady states, thus, turbulence is in a fully developed regime. Figures 2(a) and 2(b) show the time averaged steady state profiles of pressure and radial electric field $E_r = -\partial\langle\phi\rangle/\partial r$ at different power levels, respectively. Here, the power level $P_{in} = 1$ means $S_0 = 4.0 \times 10^{-5}$ at $x = 0.4$ in Fig. 1(b). It can be seen clearly that the pressure profile abruptly steepens and a deep E_r well appears when the power exceeds a threshold value ($P_{in} = 0.5 \to 1.0$), implying a transport bifurcation. This bifurcation can be attributed to strongly increased $\boldsymbol{E} \times \boldsymbol{B}$ flow shear and the resulting suppression of turbulence.[3] The $\boldsymbol{E} \times \boldsymbol{B}$ shear is set by radial force balance (i.e., the last term on the right-hand side of Eq. (1)). In fact, we have observed that for small μ_{neo}, an ETB does not form. Regarding the steep profile gradient of μ_{neo}, we have confirmed that this is not as important to ETB formation as the value of the parameter itself. We also observe that large $\boldsymbol{E} \times \boldsymbol{B}$ flow shear at the edge is triggered by the turbulence, which develops from the core due to linear instability of the steepened profiles. The critical pressure gradient for the instability is found to be about 23% of the ideal pressure gradient limit.

Figure 3 plots the power versus $-\nabla P$ curve, which indicates a transition point near $P_{in} \sim 0.6$, where the slope is
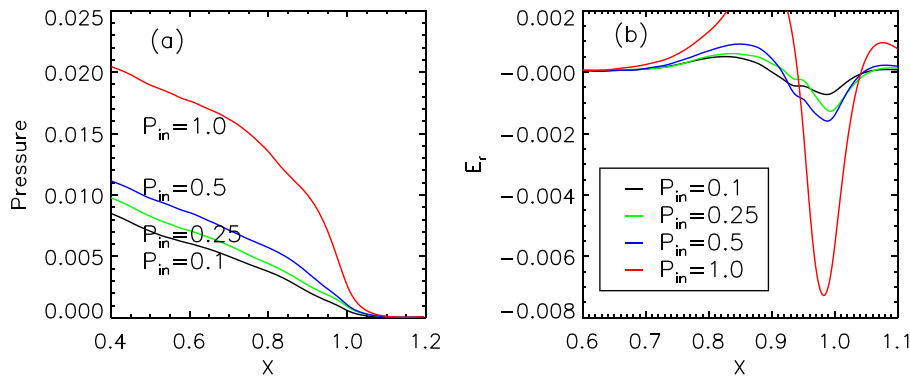
FIG. 2. Time averaged pressure (a) and radial electric field (b) profiles at different power levels.

discontinuous. This discontinuity in slope realizes a key feature of the first-order phase transition.

Note that the results in Figs. 2 and 3 are obtained at constant power. In order to get more insight into ETB transition dynamics, we have also performed a slow power ramp-up simulation. Here, power ramp-up simulation is deliberately initiated from a steady state a little below a transition point near $P_{in} \sim 0.6$ because our interest here is to observe ETB transition dynamics during a time period across a transition point. As shown in Fig. 4(a) in a green line, we start from a steady state profile obtained at $P_{in} = 0.5$ and maintain the same power level until $t = 700$. After that, the power level is slowly increased across a transition point near $P_{in} \sim 0.6$ as indicated in Fig. 3. Figures 4(a) and 4(b) plot time traces of turbulence intensity and $E \times B$ flow shear $\langle V_{E \times B} \rangle'$, respectively. These clearly show that the turbulence collapses and $E \times B$ flow shear increases rapidly at $t = t_R$ and ETB forms after this time. Results also show that there is an LCO-like phase, i.e., coherent oscillations prior to the peak of the $E \times B$ flow shear (indicated by the dashed vertical line at $t = t_R$ in Figs. 4(a) and 4(b)). This has features of a limit cycle oscillation, as predicted by predator-prey type models[12,14,16] and subsequently observed in various experiments.[8,9] Moreover, Fig. 4(c) shows that there is a phase delay of $\sim \pi/2$ between turbulence intensity and the $E \times B$ flow shear during the LCO-like phase. Rotation direction as indicated by arrow in Fig. 4(c) implies that turbulence intensity evolution leads that of $E \times B$ flow shear. This observation strongly suggests that during most of the LCO-like

phase, the $E \times B$ flow shear is dominantly due to turbulence-driven flow shear. The turbulence collapse time coincides well with the peak of the $E \times B$ flow shear at $t = t_R$.

IV. ROLE OF TURBULENCE-DRIVEN FLOW IN TRIGGERING THE ETB FORMATION

A central goal of this work is to obtain a better understanding of ETB transition evolution (in particular, the role of turbulence-driven flows in the dynamics). To this end, we calculate the normalized rate of Reynolds power R_T defined as[4–6]
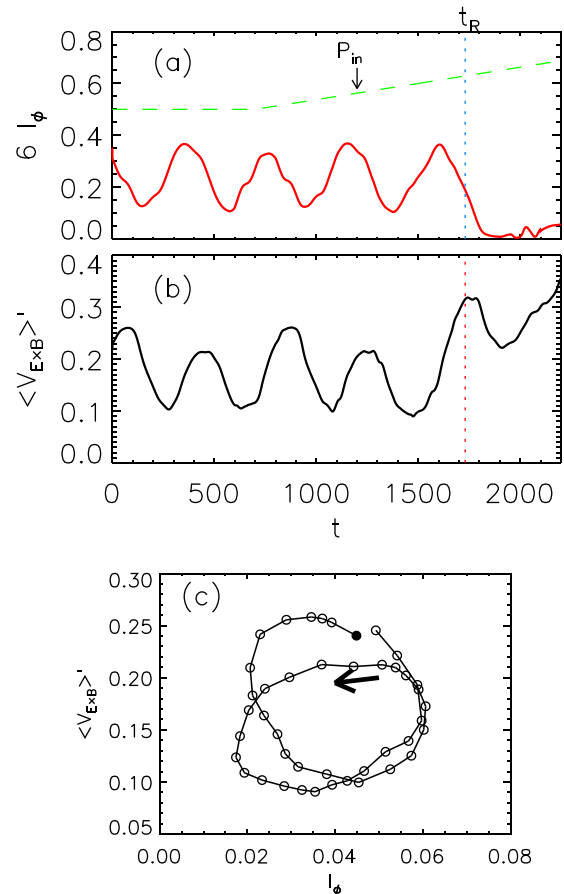

FIG. 3. Input power versus $-\nabla P$ showing a feature of the first order phase transition.

FIG. 4. Time traces of input power P_{in} and turbulence intensity $I_\phi = 10^8 \langle \tilde{\phi}^2 \rangle'$ (a) and $E \times B$ flow shear $\langle V_{E \times B} \rangle'$ at $x = 0.96$; (c) I_ϕ vs. $\langle V_{E \times B} \rangle'$ during $t = 820 - 1660$. In (c), arrow indicates that the limit cycle rotates counterclockwise as a function of time, and the filled circular point denotes the initial point at t = 820.
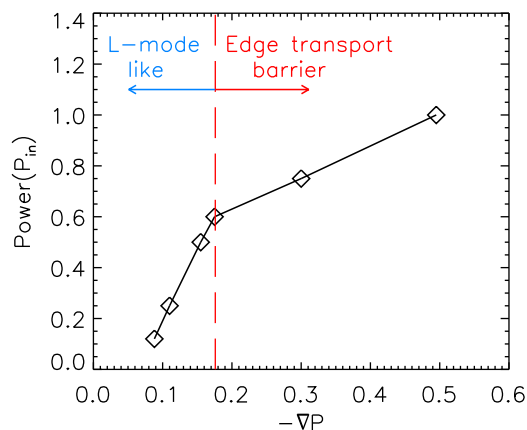
$$R_T = \frac{\langle \tilde{v}_r \tilde{v}_\theta \rangle \langle V_{E \times B}^{LF} \rangle'}{\gamma_{eff} \langle \tilde{v}_\perp^2 \rangle}, \qquad (2)$$

where $\langle \tilde{v}_r \tilde{v}_\theta \rangle$ is Reynolds stress, $\langle V_{E \times B}^{LF} \rangle$ is the $(m, n) = (0, 0)$ component of low-frequency $\boldsymbol{E} \times \boldsymbol{B}$ velocity, and $\gamma_{eff} \langle \tilde{v}_\perp^2 \rangle$ corresponds to an effective increment rate of turbulence intensity. Turbulence collapse and the transition to an ETB require $R_T > 1$, at which point the flow extracts energy from the turbulence at a rate faster than that at which the turbulence grows. In Fig. 5, we present a temporal plot of R_T. A peak of R_T appears at $t = t_R$ and coincides with the peak in the $\boldsymbol{E} \times \boldsymbol{B}$ flow shear in Fig. 4(b), when $R_T > 1$. Therefore, turbulence suppression here is caused by the sudden increase in $\boldsymbol{E} \times \boldsymbol{B}$ flow shear at the expense of turbulence energy, via the Reynolds work done on the $\boldsymbol{E} \times \boldsymbol{B}$ flow. The transition dynamics is qualitatively consistent with the experimental results of Refs. 4–7 and 31, and supports the $R_T > 1$ collapse criterion.

Figure 6 plots time traces of space and time-averaged pressure gradient $|\nabla P|$, $\boldsymbol{E} \times \boldsymbol{B}$ shearing rate $\omega_{E \times B} = |(RB_\theta/B)(V_{E \times B}B/RB_\theta)'|$,[32] and global linear growth rate γ_{lin} evaluated around the maximum radial point of $|\nabla P|$. Note that the peak of the $\boldsymbol{E} \times \boldsymbol{B}$ shearing rate at $t = t_R$ leads to that of the pressure gradient $|\nabla P|$ between $t = t_R$ and $t = t_P$. The time sequence of $|\nabla P|$ and $\omega_{E \times B}$ in Fig. 6 implies that the $\boldsymbol{E} \times \boldsymbol{B}$ flow shear burst after the LCO-like phase causes an increase in pressure gradient, which subsequently induces a further increase in mean flow shear and so activates the positive feedback loop between pressure gradient and the $\boldsymbol{E} \times \boldsymbol{B}$ shearing rate. The peak in $\omega_{E \times B}$ at $t = t_R$ results from the turbulence-driven flow shearing rate, because it occurs prior to any significant enhancement of the pressure gradient. The subsequent increase in $\omega_{E \times B}$ after $t = t_P$ is strongly correlated with that of $|\nabla P|$ and results from mean flow shear due to ∇P. Thus, we can conclude that the positive feedback loop between pressure gradient and mean flow shear begins at $t = t_P$. Notice that after reaching its peak at $t = t_R$, the $\boldsymbol{E} \times \boldsymbol{B}$ shearing rate returns to its original level at $t = t_P$. On the other hand, the pressure gradient shows a finite peak between $t = t_R$ and $t = t_P$ but does not drop to its original size at $t = t_P$. Instead, a finite residual difference between the pressure gradients before $t = t_R$ and at
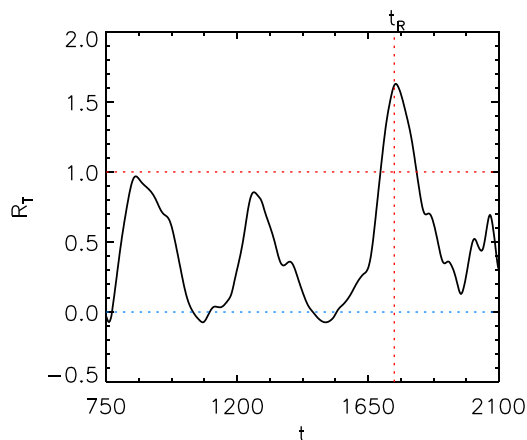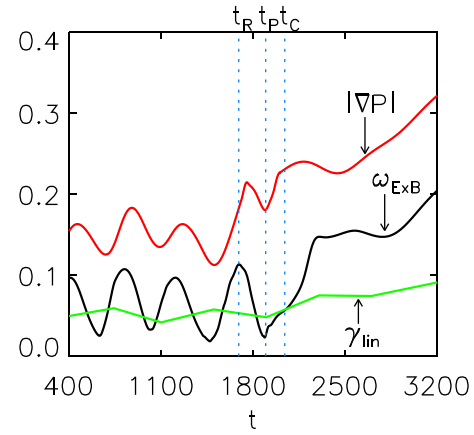
FIG. 6. Time traces of space and time-averaged $|\nabla P|$, $\omega_{E \times B}$, and γ_{lin} around the maximum radial point of $|\nabla P|$. $t = t_C$ denotes time when $\omega_{E \times B} > \gamma_{lin}$ is satisfied. Turbulence collapse occurs at t_R. Positive feedback between pressure gradient and mean flow shear begins at $t = t_P$.

$t = t_P$ is evident. This observation strongly suggests that the ETB transition has already occurred by the time $t = t_P$. The linear growth rate also drops below the $\boldsymbol{E} \times \boldsymbol{B}$ shearing rate *after* $t = t_C$, $(t_C > t_P > t_R)$ in accord with the conventional transition criterion $\omega_{E \times B} > \gamma_{lin}$.[33] Thus, we conclude that the peak of the Reynolds work (in Fig. 5) and the associated increase in the turbulence-driven flow shear are the trigger of the ETB transition. The positive feedback loop between ∇P and $\omega_{E \times B}$ develops *after* this. The drop of the linear growth rate below the $\boldsymbol{E} \times \boldsymbol{B}$ shearing rate $(\omega_{E \times B} > \gamma_{lin})$ occurs even later.

A recent paper by Cziegler *et al.*[35] has presented results of detailed quantitative analyses of the L → H transition in Alcator C-Mod using a gas-puff-imaging (GPI) diagnostics. Results show that the nonlinear exchange of kinetic energy between ambient turbulence and shear flow increases near the transition, and the suppression of turbulence when $R_T > 1$, as shown in Fig. 5. Their study has also shown that a steep profile gradient develops *after* the transient burst of the turbulence-driven zonal flow, thus establishing the time sequence of the L → H transition, i.e., $R_T > 1$ → suppression of the turbulence → increase in the mean flow shear (due to an elevated pressure gradient) to sustain the H-mode. Fig. 6 matches qualitatively this temporal sequence of the transition.

V. CONCLUSION

In conclusion, these simulation studies have elucidated the time evolution of ETB formation. The simulation accounts for the effects of self-consistent neoclassical poloidal rotation damping on radial electric field dynamics. A slow power ramp-up simulation shows that the transition to ETB is triggered by a sudden increase in the turbulence-driven flow at the expense of turbulence energy, thus allowing the pressure gradient and associated mean flow shear to rapidly increase. This result is consistent with the prediction of predator-prey models[12,14,16] and recent experiments.[31] A key observation here is that the ETB transition occurs when the normalized Reynolds work reaches a peak above unity

FIG. 5. Time traces of R_T at $x = 0.96$.

($R_T > 1$), at time t_R. The time t_R leads the time of mean flow shear development, and the standard mean shear criterion ($\omega_{E \times B} > \gamma_{lin}$) is satisfied only after $t = t_C$ ($> t_R$). This time sequence of the transition agrees with that obtained from quantitative analysis of experimental L →H transition events in Ref. 35. Therefore, we can conclude that two criteria should be satisfied (sequentially) to enter a H-mode safely: (1) $R_T > 1$ to trigger the L →H transition and (2) $\omega_{E \times B} > \gamma_{lin}$ for the sustainment of steady H-mode. This result suggests that a predictive model of the power threshold for access to H-mode must address the microscopic transition physics embedded in the $R_T > 1$ criterion, in addition to the conventional $\omega_{E \times B} > \gamma_{lin}$ one.[34] At present, it is not clear which one of the above two criteria is more important in determining the macroscopic L → H power threshold. Elucidation of microscopic parameter trends in R_T and their relation to empirical power threshold scaling is left for future work. Finally, even though the understanding of the dependence of the transition on the input parameters is important, it is missing in this study. Actually, some initial preliminary study has already shown that transition threshold power is decreased as $\nu_{i,*}$ is reduced. The change of transport coefficients ($\chi_\perp$) mainly leads to the variation of the discontinuity of slopes at the transition point in Fig. 3, while the transition threshold power does not change much. Detailed parametric dependence of the transition will be reported in future papers.

ACKNOWLEDGMENTS

[1] F. Wagner, G. Becker, K. Behringer, D. Campbell, A. Eberhagen, W. Engelhardt, G. Fussmann, O. Gehre, J. Gernhardt, G. v. Gierke, G. Haas, M. Huang, F. Karger, M. Keilhacker, O. Klüber, M. Kornherr, K. Lackner, G. Lisitano, G. G. Lister, H. M. Mayer, D. Meisel, E. R. Müller, H. Murmann, H. Niedermeyer, W. Poschenrieder, H. Rapp, H. Röhr, F. Schneider, G. Siller, E. Speth, A. Stäbler, K. H. Steuer, G. Venus, O. Vollmer, and Z. Yü, Phys. Rev. Lett. **49**, 1408 (1982).
[2] H. Biglari, P. H. Diamond, and P. W. Terry, Phys. Fluids B **2**, 1 (1990).
[3] K. H. Burrell, Phys. Plasmas **4**, 1499 (1997).
[4] P. Manz, G. S. Xu, B. N. Wan, H. Q. Wang, H. Y. Guo, I. Cziegler, N. Fedorczak, C. Holland, S. H. Müller, S. C. Thakur, M. Xu, K. Miki, P. H. Diamond, and G. R. Tynan, Phys. Plasmas **19**, 072311 (2012).
[5] G. R. Tynan, M. Xu, P. H. Diamond, J. A. Boedo, I. Cziegler, N. Fedorczak, P. Manz, K. Miki, S. Thakur, L. Schmitz, L. Zeng, E. J. Doyle, G. M. Mckee, Z. Yan, G. S. Xu, B. N. Wan, H. Q. Wang, H. Y. Guo, J. Dong, K. Zhao, J. Cheng, W. Y. Hong, and L. W. Yan, Nucl. Fusion **53**, 073053 (2013).
[6] I. Shesterikov, Y. Xu, G. R. Tynan, P. H. Diamond, S. Jachmich, P. Dumortier, M. Vergote, M. Van Schoor, G. Van Oost, and TEXTOR Team, Phys. Rev. Lett. **111**, 055006 (2013).
[7] I. Cziegler, P. H. Diamond, N. Fedorczak, P. Manz, G. R. Tynan, M. Xu, R. M. Churchill, A. E. Hubbard, B. Lipschultz, J. M. Sierchio, J. L. Terry, and C. Theiler, Phys. Plasmas **20**, 055904 (2013).
[8] T. Estrada, C. Hidalgo, T. Happel, and P. H. Diamond, Phys. Rev. Lett. **107**, 245004 (2011).
[9] L. Schmitz, L. Zeng, T. L. Rhodes, J. C. Hillesheim, E. J. Doyle, R. J. Groebner, W. A. Peebles, K. H. Burrell, and G. Wang, Phys. Rev. Lett. **108**, 155002 (2012).
[10] D. G. Dritschel and M. E. McIntyre, J. Atmos. Sci. **65**, 855 (2008).
[11] F. L. Hinton, Phys. Fluids B **3**, 696 (1991).
[12] P. H. Diamond, Y. M. Liang, B. A. Carreras, and P. W. Terry, Phys. Rev. Lett. **72**, 2565 (1994).
[13] B. N. Rogers, J. F. Drake, and A. Zeiler, Phys. Rev. Lett. **81**, 4396 (1998).
[14] E.-J. Kim and P. H. Diamond, Phys. Rev. Lett. **90**, 185006 (2003).
[15] A. Thyagaraja, M. Valovic, and P. J. Knight, Phys. Plasmas **17**, 042507 (2010).
[16] K. Miki, P. H. Diamond, Ö. D. Gürcan, G. R. Tynan, T. Estrada, L. Schmitz, and G. S. Xu, Phys. Plasmas **19**, 092306 (2012).
[17] W. Fundamensi, F. Militello, D. Moulton, and D. C. McDonald, Nucl. Fusion **52**, 062003 (2012).
[18] L. Chone, P. Beyer, Y. Sarazin, G. Fhur, C. Bourdelle, and S. Benkadda, Phys. Plasmas **21**, 070702 (2014).
[19] J. Cheng, J. Q. Dong, K. Itoh, L. W. Yan, M. Xu, K. J. Zhao, W. Y. Hong, Z. H. Huang, X. Q. Ji, W. L. Zhong, D. L. Yu, S.-I. Itoh, L. Nie, D. F. Kong, T. Lan, A. D. Liu, X. L. Zou, Q. W. Yang, X. T. Ding, X. R. Duan, Yong Liu, and HL-2A Team, Phys. Rev. Lett. **110**, 265002 (2013).
[20] T. Kobayashi, K. Itoh, T. Ido, K. Kamiya, S.-I. Itoh, Y. Miura, Y. Nagashima, A. Fujisawa, S. Inagaki, K. Ida, and K. Hoshino, Phys. Rev. Lett. **111**, 035002 (2013).
[21] P. Beyer, S. Benkadda, G. Fhur-Chaudier, X. Garbet, Ph. Ghendrih, and Y. Sarazin, Plasma Phys. Controlled Fusion **49**, 507 (2007).
[22] M. Becoulet, F. Orain, P. Maget, N. Mellet, X. Garbet, E. Nardon, G. T. A. Huysmans, T. Casper, A. Loarte, P. Cahyna, A. Smolyakov, F. L. Waelbroeck, M. Schaffer, T. Evans, Y. Liang, O. Schmitz, M. Beurskens, V. Rozhansky, and E. Kaveeva, Nucl. Fusion **52**, 054003 (2012).
[23] T. A. Gianakon, S. E. Kruger, and C. C. Hegna, Phys. Plasmas **9**, 536 (2002).
[24] X. Garbet, C. Bourdelle, G. T. Hoang, P. Maget, S. Benkadda, P. Beyer, C. Figarella, I. Voitsekovitch, O. Agullo, and N. Bian, Phys. Plasmas **8**, 2793 (2001).
[25] B. D. Dudson, H. R. Wilson, M. V. Umansky, X. Q. Xu, and P. B. Snyder, Comput. Phys. Commun. **180**, 1467 (2009).
[26] X. Q. Xu, W. M. Nevins, R. H. Cohen, J. R. Myra, and P. B. Snyder, New J. Phys. **4**, 53 (2002).
[27] X. Q. Xu, R. H. Cohen, T. D. Rognlien, and J. R. Myra, Phys. Plasmas **7**, 1951 (2000).
[28] F. L. Hinton and R. D. Hazeltine, Rev. Mod. Phys. **48**, 239 (1976).
[29] Y. B. Kim, P. H. Diamond, and R. J. Groebner, Phys. Fluids B **3**, 2050 (1991).
[30] Even though we choose one particular form of source profile as depicted in Fig. 1(b), we have checked that the main simulation result does not depend on the detailed source profile forms used in the simulation.
[31] Z. Yan, G. R. McKee, R. Fonck, P. Gohil, R. J. Groebner, and T. H. Osborne, Phys. Rev. Lett. **112**, 125002 (2014).
[32] T. S. Hahm and K. H. Burrell, Phys. Plasmas **2**, 1648 (1995).
[33] R. E. Waltz, G. D. Kerbel, and J. Milovitch, Phys. Plasmas **1**, 2229 (1994).
[34] R. Singh, H. Jhang, P. K. Kaw, P. H. Diamond, H. Nordman, C. Bourdelle, and A. Loarte, Phys. Plasmas **21**, 062503 (2014).
[35] I. Cziegler *et al.*, Plasma Phys. Controlled Fusion **56**, 075013 (2014).